JACS
JOURNAL OF THE AMERICAN CHEMICAL SOCIETY
Article
pubs.acs.org/JACS

Water Oxidation Catalysis: Electrocatalytic Response to Metal Stoichiometry in Amorphous Metal Oxide Films Containing Iron, Cobalt, and Nickel

Rodney D. L. Smith,[†] Mathieu S. Prévot,[†] Randal D. Fagan,[†] Simon Trudel,*[,†,‡,§] and Curtis P. Berlinguette*[,†,‡,⊥]

[†]Department of Chemistry, [‡]Centre for Advanced Solar Materials, and [§]Institute for Quantum Science and Technology, University of Calgary, 2500 University Drive NW, Calgary T2N 1N4, Canada

[⊥]Departments of Chemistry and Chemical and Biological Engineering, The University of British Columbia, 2036 Main Mall, Vancouver, BC V6T 1Z1, Canada

Supporting Information

ABSTRACT: Photochemical metal−organic deposition (PMOD) was used to prepare amorphous metal oxide films containing specific concentrations of iron, cobalt, and nickel to study how metal composition affects heterogeneous electrocatalytic water oxidation. Characterization of the films by energy-dispersive X-ray spectroscopy and X-ray photoelectron spectroscopy confirmed excellent stoichiometric control of each of the 21 complex metal oxide films investigated. In studying the electrochemical oxidation of water catalyzed by the respective films, it was found that small concentrations of iron produced a significant improvement in Tafel slopes and that cobalt or nickel were critical in lowering the voltage at which catalysis commences. The best catalytic parameters of the series were obtained for the film of composition *a*-$Fe_{20}Ni_{80}$. An extrapolation of the electrochemical and XPS data indicates the optimal behavior of this binary film to be a manifestation of iron stabilizing nickel in a higher oxidation level. This work represents the first mechanistic study of amorphous phases of binary and ternary metal oxides for use as water oxidation catalysts, and provides the foundation for the broad exploration of other mixed-metal oxide combinations.

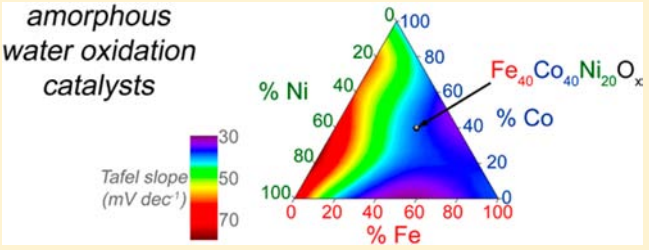

INTRODUCTION

Amorphous metal oxides have garnered significant recent attention for their role in catalyzing the oxygen evolving reaction (OER), a key half-reaction associated with the electrolysis of water.[1,2] While there is a vast body of literature centered on metals,[3] metal alloys,[4,5] and crystalline metal oxides,[6,7] amorphous metal oxides have, until recently, received far less attention despite their proven utility as OER catalysts. One issue suppressing the extensive development of amorphous materials is the limited availability of methods capable of accessing complex compositions. While anodic electrodeposition, for example, is amenable to oxides consisting of certain metals (e.g., Fe,[8] Pb,[9] Co,[9,10] Ni,[11] Ir,[12,13] Ru,[14,15] Mn,[16]), it does not translate effectively to all metal oxides (e.g., amorphous IrO_x has only been prepared through the electrolytic decomposition of an organometallic precursor[12,13]). Perhaps an even greater shortcoming is the challenge in producing a uniform distribution of different metal ions within an amorphous metal oxide film. Indeed, binary metal oxide amorphous films typically have a metal content that differs from the stoichiometry of the precursor solutions employed.[8,9] One illustrative example is the finding that the electrodeposition from a precursor solution containing a 1:1 molar ratio of Fe and Ni produces a film with an Fe:Ni ratio of 1:2 to 1:2.6, depending on the deposition parameters.[8] Other techniques have been successfully employed to prepare amorphous binary metal oxide films (e.g., hydrothermal techniques for Mn−Ca oxide;[16,17] cosputtering of Ta−Ni oxide;[18] thermal decomposition for Ir−Ru oxide[15]), but these methods also do not necessarily translate to all metal identities nor do they circumvent undesirable segregation.

We recently reported a versatile technique, photochemical metal−organic depositions (PMOD),[19−21] for accessing amorphous mixed-metal oxide OER catalysts.[22] PMOD is a scalable, low-cost technique capable of producing amorphous metal oxides for OER catalysis with precise metal compositions. This Article elaborates on our earlier report by examining a series of amorphous ternary metal oxides containing well-defined compositions of Fe, Co, and Ni to probe how specific metal stoichiometries affect various catalytic parameters that are relevant to OER catalysis. Identification of how each metal affects catalytic activity provides the basis for an empirical model to enable the rational design of OER catalysts. While this

Received: March 28, 2013
Published: July 24, 2013

   dx.doi.org/10.1021/ja403102j | J. Am. Chem. Soc. 2013, 135, 11580−11586

type of analysis on crystalline OER catalysts has had a lasting influence on the design of crystalline oxides (e.g., see seminal work of Bockris[6] showing a linear relationship between electrocatalytic activity and the heat of formation of metal hydroxides, and that of Trassati[23] establishing a linear relationship between the catalytic activity and the enthalpy of the lower to higher metal-oxide oxidation state transition [e.g., Ni(II) to Ni(III)]), there currently is no such analysis in the literature describing amorphous phases. This examination of mixed-metal oxides containing iron, cobalt, and nickel is therefore an important starting point for such an analysis for amorphous films.

EXPERIMENTAL SECTION

Film Preparation. Solutions of metal precursor complexes were prepared by dissolving the appropriate ratio of metal complexes in hexanes to achieve an overall 15% w/w solution. Precursor solutions used include iron(III) 2-ethylhexanoate (50% w/w in mineral spirits, Strem Chemicals), cobalt(II) 2-ethylhexanoate (65% w/w in mineral spirits, Alfa Aesar), and nickel(II) 2-ethylhexanoate (78% w/w in 2-ethylhexanoic acid, Strem Chemicals). Films of the precursor complexes were prepared by spin-coating at 3000 rpm for 60 s (Laurell model WS-650MZ-23NPP-Lite). Films were then irradiated under UV light (Atlantic Ultraviolet G18T5VH/U lamp, 185/254 nm) and annealed at 100 °C for 1 h. As previously reported, infrared spectroscopy can be employed to follow the photochemical decomposition of metal−organic complex thin films.[20,24,25] The reactions are judged complete when the bands due to the C−H (2800−3000 cm^{-1}) and C═O (~1680 cm^{-1}) vibrations disappear, as shown for cobalt films in Figure SI1. Films were prepared on fluorine-doped tin oxide (FTO) glass (electrochemical experiments), silicon wafers (for SEM imaging), or KBr discs (to follow the reaction by IR spectroscopy).

Electrochemistry. Electrochemical measurements were performed using a CH Instrument Workstation 660D potentiostat. All measurements were carried out in 0.1 M KOH. A standard three-compartment electrochemical cell was used, with a Luggin capillary joining the reference electrode to the working electrode compartment, and a porous glass frit separating the working electrode and counter electrode compartments. A Pt mesh was used as a counter electrode. Calibration of a Ag/AgCl (sat. KCl) electrode against a 1 mM aqueous solution of $Na_4[Fe(CN)_6]$ indicated the reference electrode had a potential of +0.126 V vs NHE. All electrochemical potentials were corrected for uncompensated resistance (R_u) and are given in the text relative to the reversible hydrogen electrode (vs RHE):

$$E_{RHE} = E + 0.126 + 0.059 \cdot pH - iR_u \quad (1)$$

Tafel plots were acquired, in triplicate, through staircase voltammetry (10 mV steps, 50 s intervals). Values given in the text represent the average between all electrodes of a given composition.

Scanning Electron Microscopy. Scanning electron microscopy (SEM) and energy-dispersive X-ray spectroscopy (EDXS) were performed using a Zeiss Σigma VP field emission scanning electron microscope equipped with an Oxford INCA X-Act EDXS unit.

X-ray Photoelectron Spectroscopy. A Physical Electronics PHI VersaProbe 5000-XPS was used to record XPS spectra (Catalysis Surface Science Laboratory, University of Calgary). The spectra were acquired using a monochromatic Al K_α source (1486.6 eV, 49.3 W) and beam diameter of 200.0 μm. A double neutralization (low energy electron beam and low energy Ar^+ beam) was used during spectrum acquisition. For each sample, a survey scan (0−1350 eV, Figures SI2−SI8) was performed to determine elemental composition. Survey scans indicated the presence of carbon in all of the samples, and occasionally tin from the underlying FTO substrate. The observation of carbon at the film surface has previously been observed by XPS and Auger spectroscopy in PMOD-prepared films. The carbon was shown to be surface contamination and not residual unreacted ligand, as ion-sputtering of the surface resulted in the removal of carbon.[24−27] Evidence that this was also the case for the current results is provided in Figure SI9, where ion-sputtering of a-$Fe_{40}Co_{40}Ni_{20}O_x$ resulted in complete removal of carbon. Ion-sputtering was not used in the current work as preferential sputtering of oxygen is known to alter the oxidation states of iron, cobalt, and nickel oxide and hydroxide species,[28−30] and as such sputtering may yield misleading information about the speciation of catalytically relevant surface species. The tin signal, when observed, is weak and is believed to be due to the FTO surface being exposed by cracks in the film. The survey scan was followed by a high sensitivity scan collected with a pass energy of 23.50 eV. The absence of carbon is supported by the disappearance of all C−H and C═O signals in the IR spectra.

All spectra analyses were performed using CasaXPS. Spectra were corrected by calibrating all peaks to the major adventitious C 1s signal (284.8 eV). A Shirley-type background was used, and spectra were fitted using peaks with a GL(30) profile. An adaptation of literature procedures was used for peak fitting; details are given in the Supporting Information.[31−34]

RESULTS AND DISCUSSION

Film Preparation, Composition, and Morphology. A series of 21 amorphous mixed-metal oxide films formulated as a-$Fe_{100-y-z}Co_yNi_zO_x$, where y and z were each varied from 0 to 100 in 20-step increments (Figure 1), were prepared by the

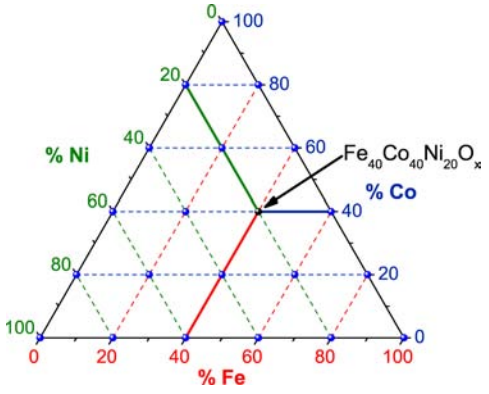

Figure 1. Diagram of compositions depicting the (mixed-)metal oxide films examined in this work. Circles at vertices represent the nominal compositions of the films. An illustrative film composition is indicated by the black circle.

PMOD method as described previously.[22] Briefly, a spin-cast film of the appropriate metal−organic precursor complexes was photolyzed and then annealed for 1 h at 100 °C to produce amorphous metal oxide films. Metal oxide films prepared by this approach were previously measured to be approximately 150−200 nm in thickness.[22] Of the 21 films, seven representative samples (three pure metal oxides, three binary compositions, and one ternary oxide) were interrogated at higher levels of sophistication; experimental details are provided in Table 1.

Elemental compositions of the selected films were determined by both EDXS and XPS. Results from both techniques were in excellent agreement with the metal compositions of the corresponding precursor solutions (Table 1). EDXS measurements were performed at no less than five different locations on the surfaces of the films. The results confirmed that each film possessed a reasonably uniform metal composition over the entire film. The standard deviation between measurements, given as the error values in Table 1, was between 1% and 3% for all four mixed-metal oxide samples. Because EDXS probes the films at greater depths (~1−5 μm)

dx.doi.org/10.1021/ja403102j | J. Am. Chem. Soc. 2013, 135, 11580−11586

Table 1. Elemental Analysis of Amorphous Metal Oxide Films Determined by EDXS and XPS

	calcd[a] (at. %)			found (at. %)		
nominal composition	Fe	Co	Ni	Fe	Co	Ni
Recorded on Si[b]						
a-$Fe_{40}Co_{60}O_x$	41	59		38 ± 1	62 ± 1	
a-$Fe_{40}Ni_{60}O_x$	39		61	34 ± 3		66 ± 3
a-$Co_{40}Ni_{60}O_x$		41	59		39 ± 1	61 ± 1
a-$Fe_{40}Co_{40}Ni_{20}O_x$	39	39	22	39 ± 2	42 ± 2	19 ± 2
Recorded on FTO[c]						
a-$Fe_{40}Co_{60}O_x$	36	64		35	65	
a-$Fe_{40}Ni_{60}O_x$	39		61	32		68
a-$Co_{40}Ni_{60}O_x$		41	59		35	65
a-$Fe_{40}Co_{40}Ni_{20}O_x$	39	39	22	34	46	20

[a]Based on relative molar ratios of metal 2-ethylhexanoate precursors. [b]EDXS data recorded on catalyst films deposited on Si wafers; error bars represent the standard deviation between a minimum of five points on the electrode surface. [c]XPS data recorded on catalyst films deposited on FTO glass.

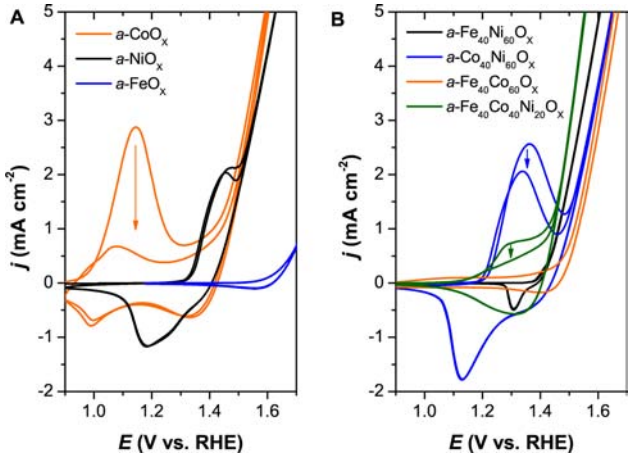

Figure 3. Cyclic voltammograms of amorphous metal oxides films containing (A) single or (B) mixed-metal oxide compositions. Data were collected at a scan rate of 10 mV s^{-1} in 0.1 M KOH. Arrows indicate progression of scans.

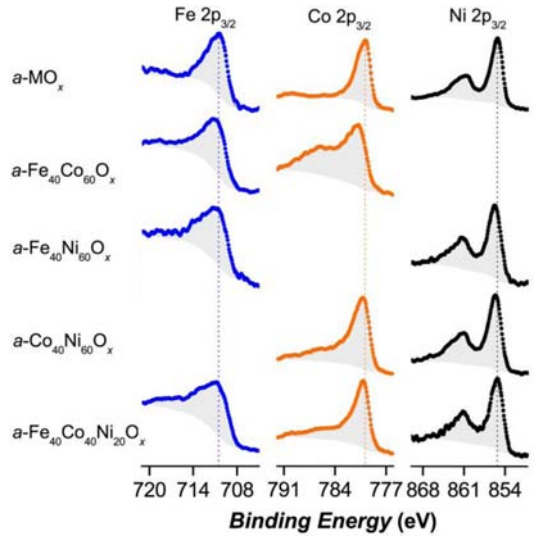

Figure 4. Iron (blue), cobalt (orange), and nickel (black) $2p_{3/2}$ regions of XPS spectra recorded on four mixed-metal oxide films. Spectra for a-FeO_x, a-CoO_x, and a-NiO_x are provided for comparison.

than XPS (~50 Å), the alignment in experimental values to expected compositions for both techniques corroborates a homogeneous metal distribution within the entire film. This outcome highlights the acute control of metal stoichiometry in amorphous mixed-metal oxide films offered by the PMOD technique.

Scanning electron microscopy (SEM) highlighted good coverage of the films across the entire surface of each electrode (Figure 2 and Figure SI10) with morphologies of most films comparable to those of a-FeO_x.[22] The otherwise smooth films are interrupted by a small degree of cracking along the surface in certain locations. High-magnification images reveal some variation in surface roughness was present between films of different compositions, with the most pronounced difference in morphologies observed for a-CoO_x and a-NiO_x: each of these films exhibited rougher surfaces (Figure 2).

Film Speciation. A combination of cyclic voltammetry (Figure 3) and XPS (Figure 4) was used to gain insight into the speciation and electrochemical behavior of each of the films. While modeling the photoelectron spectra of metal oxides, and particularly mixed-metal oxides,[32] can be challenging due to the presence of several overlapping features, a modulation of established curve-fitting techniques (details provided in the Supporting Information),[32,33] combined with supporting electrochemical data, should produce reasonable identification of metal species in the amorphous films.

Of the three films containing exclusively iron, cobalt, or nickel metals, only a-FeO_x lacked a precatalytic oxidation process in the cyclic voltammogram. The absence of this wave, in combination with similar XPS spectra for crystalline Fe_2O_3 and a-FeO_x,[33] strongly suggests that iron(III) sites comprise a-FeO_x. This assignment is in accordance with a recent X-ray absorption spectroscopic study of amorphous iron oxide films prepared by PMOD.[21] The O 1s region of the photoelectron spectrum for a-FeO_x indicated that ~65% of the oxygen was in the form of hydroxyl groups (531.39 eV), with the remaining

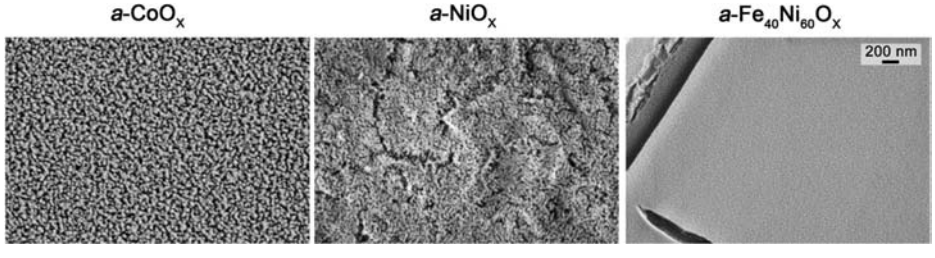

Figure 2. Scanning electron micrographs of metal oxide films deposited on silicon wafers. The 200-nm scale bar applies to all three micrographs. A comprehensive set of micrographs is provided as Supporting Information (Figure SI10).

dx.doi.org/10.1021/ja403102j | J. Am. Chem. Soc. 2013, 135, 11580−11586

35% present as lattice oxygen (O^{2-}) groups (529.69 eV). The binding energies of these two types of oxygen are in good agreement with literature values.[32] Not unexpectedly, the atomic ratio of the two forms is significantly different from that reported for crystalline Fe_2O_3, where 60% of the oxygen present is reported as lattice oxygen.[32]

An oxidative sweep of the *a*-CoO_x film produced a prominent peak at $E_{p,a}$ = +1.15 V vs RHE prior to the onset of catalysis at ca. +1.35 V. Two reduction processes at $E_{p,c}$ = +1.34 and +0.99 V were evident upon a successive cathodic sweep. The preoxidation peak was significantly diminished and shifted toward +1.08 V during successive scans. Integration of the three peaks (on the second cycle) indicated that the overall charge transferred in each of the electron-transfer processes was comparable, thus indicating that the lower intensity of the precatalytic oxidation peak was a consequence of the initial form of the material not being regenerated within the time domain of the experiment. Given that the Co $2p_{3/2}$ region of the XPS spectrum closely resembles that of the mixed-valent Co(III/II) oxide (Co_3O_4),[32] the precatalytic signal at $E_{p,a}$ = +1.15 V and associated reduction peak at $E_{p,c}$ = +0.99 V are assigned to a quasi-reversible Co(III)/Co(II) redox couple. The significant decrease in the magnitude of the precatalytic oxidation peak between the first and second cycles is presumably a consequence of poor diffusion of the electrolyte through the film on the time scale of the experiment, preventing the reduction of all of the cobalt(III) sites in the film. The $E_{p,c}$ at +1.34 V is assigned as the reduction of Co(IV) to Co(III) in view of Co(IV) recently being identified by EPR spectroscopy to be an intermediate for water oxidation by the ubiquitous Co–P_i system.[35] The Ni $2p_{3/2}$ region of the *a*-NiO_x film was fitted to peak parameters corresponding to $Ni(OH)_2$.[32] The precatalytic oxidation process at $E_{p,a}$ = +1.45 V vs RHE was therefore assigned to the oxidation of $Ni(OH)_2$ to NiOOH, with the broad reductive peak at +1.18 V on the reverse scan assigned to the regeneration of $Ni(OH)_2$ in accordance with a study by Trotochaud et al.[31]

CVs recorded on the binary metal oxide films produced substantially different behavior relative to those of the pure metal oxides (Figure 4). Oxidative scans of *a*-$Fe_{40}Co_{60}O_x$ and *a*-$Fe_{40}Ni_{60}O_x$ revealed partial to complete suppression of the precatalysis oxidation peaks (e.g., the *a*-$Fe_{40}Co_{60}O_x$ film showed only modest oxidation and reduction currents at +1.05 and 1.41 V, respectively; no precatalytic oxidation peak was measured for the *a*-$Fe_{40}Ni_{60}O_x$ film, although the cathodic sweep revealed a small rise positively shifted relative to the major reduction peak observed for *a*-NiO_x). The $2p_{3/2}$ regions of the XPS spectra for the mixed-metal oxides indicate a change in speciation for each of the metals when compared to the amorphous oxides containing a singular metal element. Although the Fe $2p_{3/2}$ envelope is similar for both *a*-$Fe_{40}Co_{60}O_x$ and *a*-$Fe_{40}Ni_{60}O_x$, the peaks were broadened and shifted to higher binding energies as compared to *a*-FeO_x. This broadening resulted in a poor fitting to the Fe_2O_3 peak parameters and a much stronger correlation to the FeOOH parameters.[33] The Ni region also displayed a positive shift and broadening in the $2p_{3/2}$ peak envelope that is indicative of NiOOH.[32] As compared to *a*-CoO_x, the Co $2p_{3/2}$ envelope for *a*-$Fe_{40}Co_{60}O_x$ was shifted nearly 1 eV higher and was accompanied by the growth of a high-energy shoulder corresponding to $Co(OH)_2$.[32]

The *a*-$Co_{40}Ni_{60}O_x$ films exhibited a precatalytic oxidation process centered at $E_{p,a}$ = +1.34 V, a value that resides between the *a*-CoO_x (+1.08 V) and *a*-NiO_x (+1.45 V) films. The CV did not display signals corresponding to either of the pure amorphous oxides. The sharpness of the reduction signal at $E_{p,c}$ = +1.13 V on the reverse sweep suggests a single electron-transfer process that is difficult to unambiguously assign. Further complicating matters is the fact that the Co region of the photoelectron spectrum did not match any single known cobalt oxide species, although a fit could be obtained for a mixture of 57% $Co(OH)_2$ and 43% Co_3O_4 (with the caveat that this model considered multiple, overlapping signals).[32] Curve fitting of the Ni region of the spectrum for *a*-$Fe_{40}Ni_{60}O_x$ corresponded to the $Ni(OH)_2$ phase.[32] Taking into collective consideration the XPS data and the observation that *a*-NiO_x produces much larger oxidation/reduction peaks than *a*-CoO_x, we ascribe the strong precatalytic oxidation/reduction signals observed in the CVs of *a*-$Co_{40}Ni_{60}O_x$ to the interconversion between $Ni(OH)_2$ and NiOOH, with the cobalt remaining electrochemically benign.

The ternary mixture *a*-$Fe_{40}Co_{40}Ni_{20}O_x$ showed electrochemical behavior similar to that of *a*-$Co_{40}Ni_{60}O_x$. XPS data of the films indicate that the iron sites exist as the FeOOH form, nickel as $Ni(OH)_2$, and roughly equivalent concentrations of cobalt as Co_3O_4 and $Co(OH)_2$. On the grounds that Co_3O_4, FeOOH in *a*-$Fe_{40}Ni_{60}O_x$ and *a*-$Fe_{40}Co_{60}O_x$, and $Co(OH)_2$ in *a*-$Fe_{40}Co_{60}O_x$ are all electrochemically silent over this region, the precatalytic oxidation process of the ternary film is ascribed to the redox activity of the nickel centers, the oxidation of $Ni(OH)_2$ to NiOOH. This NiOOH phase is not susceptible to electrochemical reduction and thus does not regenerate the $Ni(OH)_2$ phase, which reflects the suppression of the precatalytic phase during subsequent scans.

Oxygen Evolution Kinetics. An understanding of how kinetics factored into the electrochemical behavior was provided by a comparison of the Tafel plots (Figure 5).

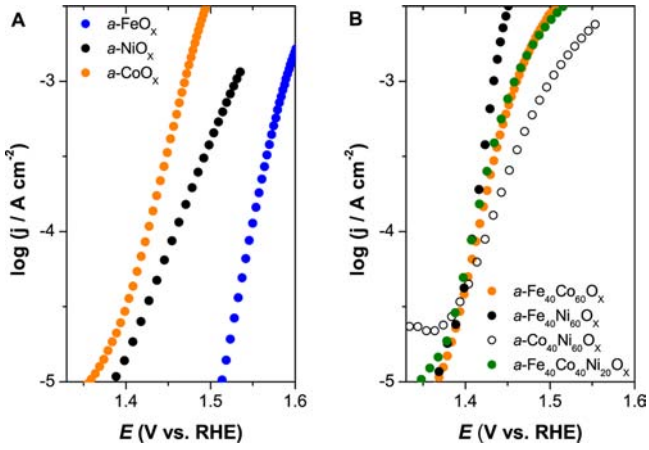

Figure 5. Tafel plots obtained for (A) pure metal oxides and (B) mixed-metal oxides prepared by PMOD. Measurements performed in 0.1 M KOH(aq).

Three kinetic parameters were selected to benchmark catalyst performance: (i) overpotential (η) where the linear Tafel region begins (referred herein as "onset η"); (ii) Tafel slope (mV dec^{-1}); and (iii) η required to reach a current density of 0.5 mA cm^{-2} (Figure 6 and Table 2). The latter parameter is an extensively used literature benchmark, but does not accurately represent the intrinsic catalytic properties of the materials studied here due to the inherent difficulty of accurately

dx.doi.org/10.1021/ja403102j | J. Am. Chem. Soc. 2013, 135, 11580–11586

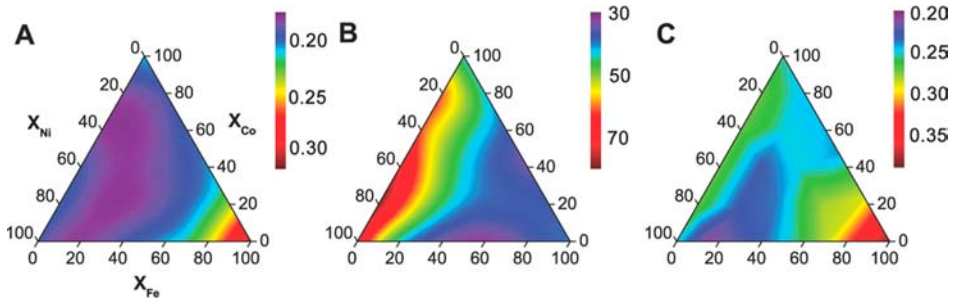

Figure 6. Contour plots of kinetic parameters extracted from Tafel plots recorded on 21 independent amorphous (mixed-) metal oxide films: (A) onset η in units of V; (B) Tafel slopes in units of mV dec^{-1}; and (C) η (in units of V) required to reach j = 0.5 mA cm^{-2}.

Table 2. Summary of Kinetic Parameters Extracted from the Tafel Plots Recorded on Selected Films

nominal compositions						
% Fe	% Co	% Ni	onset η (V)	Tafel slope (mV dec^{-1})	η @ 0.5 mA cm^{-2}	η @ 1 mA cm^{-2}
100	0	0	0.32 ± 0.02	40 ± 4	0.38 ± 0.02	0.41 ± 0.02
36	64	0	0.20 ± 0.02	40 ± 7	0.25 ± 0.01	0.27 ± 0.02
0	100	0	0.21 ± 0.02	42 ± 2	0.26 ± 0.02	0.27 ± 0.02
40	0	60	0.19 ± 0.01	34 ± 8	0.23 ± 0.01	0.25 ± 0.03
0	0	100	0.19 ± 0.01	73 ± 6	0.25 ± 0.01	0.28 ± 0.01
0	41	59	0.19 ± 0.01	73 ± 6	0.27 ± 0.00	0.30 ± 0.01
39	39	22	0.19 ± 0.00	40 ± 1	0.25 ± 0.01	0.28 ± 0.01

measuring the surface roughness of the films. We therefore contend that the onset η, an intrinsic property of the catalyst that is insensitive to data normalization, stands out as a useful comparative parameter in the context of this study.

The OER activities of a-CoO_x and a-NiO_x were far greater than that of a-FeO_x. The a-CoO_x catalyst produced by the PMOD technique also exhibits a slightly lower onset η (0.21 V) than the well-documented CoP_i catalyst (~0.25 V)[36] and an improved Tafel slope (42 vs ~60 mV dec^{-1}). The catalytic parameters of the a-CoO_x films in this Article are more comparable to those prepared by thermal decomposition.[31] The a-NiO_x film is also characterized by a lower onset η (0.19 V) than the electrodeposited amorphous Ni-borate catalyst reported by Nocera and co-workers (~0.30 V); however, an improvement in the Tafel slope was not observed.[11] We note that conditions employed in the present work, most notably the solution pH, are different from those reported for CoP_i (7)[36] and NiB_i (9.2),[11] which may contribute to the differences in reactivity.

Several trends in the kinetic parameters extracted from the mixed-metal combinations are apparent in the contour plots shown in Figure 5. The data in Figure 5A, for example, show a lower onset η when the iron concentration is maintained at 20−40% for binary and ternary films. At progressively larger concentrations of Fe, however, the onset η steadily increases until it reaches the worst value of the series (i.e., 0.32 V for a-FeO_x). No clear trends could be discerned along the Co−Ni axis of the ternary plots, suggesting that cobalt and nickel induce similar effects on the film properties.

The Tafel slopes were remarkably sensitive to the amount of iron present (Figure 5B). In the absence of iron, for example, higher concentrations of nickel were found to produce higher Tafel slopes; that is, films rich in nickel afforded Tafel slopes over the 70−80 mV dec^{-1} range, while films with a high abundance of cobalt produced slopes of ca. 60 mV dec^{-1}. The presence of iron in any of the films, however, produced Tafel slopes of 30−40 mV dec^{-1}, where an iron concentration of 40−60% generated optimal Tafel slopes for both the binary and the ternary mixtures.

A 24 h chronopotentiometry experiment with a current density of 1 mA cm^{-2} was performed to probe the stability of the amorphous mixed-metal oxide films (Figure SI12). Both a-$Fe_{40}Co_{40}Ni_{20}O_x$ and a-$Fe_{40}Ni_{60}O_x$ required only minor increases in potential to maintain the current density over this time frame. The good stability is in agreement with previous results for single-metal films.[22]

The O 1s regions of the XPS spectra were also examined for several film compositions to discern the observed trends in Tafel slopes (Figure 6). The experimental data were fit using the technique used by Trotochaud et al.,[31] where adventitious organic compounds are included in the model (see the Supporting Information), and indicate two types of oxygen in the amorphous films. The major oxygen component in each of the seven films was found to be hydroxyl surface groups according to the integration of the peak at 531.2 ± 0.2 eV, with the second highest concentration of oxygen corresponding to those that comprise the lattice (i.e., O^{2-}) based on the signal at 529.7 ± 0.2 eV.[32−34] The relative concentrations of hydroxyl surface groups to lattice oxygen for each of the films tracked the Tafel behavior; that is, a lower relative concentration of hydroxyl groups led to superior Tafel slopes (Figure SI13). For example, 98% of the oxygen in a-NiO_x, which produced a Tafel slope of 73 mV dec^{-1}, exists as hydroxides (recall that the dominant species is $Ni(OH)_2$). The Tafel slope for a-$Fe_{40}Ni_{60}O_x$, however, is only 34 mV dec^{-1}. This film contained a greater concentration of NiOOH and FeOOH, lowering the hydroxide content to 73%.

The collective XPS and electrochemical data indicate that the presence of iron in the films tends to stabilize higher oxidation levels of the metals after the initial oxidation event. This assessment is supported by (i) direct observation of variability in metal oxidation states (e.g., $Ni(OH)_2$ for a-NiO_x, but NiOOH for a-$Fe_{40}Ni_{60}O_x$); (ii) films that give rise to the lowest Tafel slopes contain the lowest abundance of hydroxyl groups

dx.doi.org/10.1021/ja403102j | J. Am. Chem. Soc. 2013, 135, 11580−11586

that, in turn, suggests a higher overall oxidation state of the film; and (iii) the disappearance of precatalytic Co and Ni oxidation peaks in CVs of films containing Fe. This behavior is aligned with recently published results from Stahl and co-workers on crystalline oxides of similar metal compositions showing a similarly beneficial role on Fe.[37] These observations hint that the addition of certain metals not yet studied in this context may stabilize higher oxidation levels of catalyst films (or decrease the relative amount of hydroxyl surface groups) providing a cogent strategy for the rational design of heterogeneous water oxidation catalysts. Such a change in the preferred oxidation state would likely shift the rate-determining step of the reaction, if not a change to a completely new reaction mechanism.[6]

The trends in the contour plot provided in Figure 5C, which tracks the overpotential necessary to achieve a current density of 0.5 mA cm^{-2}, follow the collective behavior of the onset overpotentials and Tafel slopes in Figure 5A and B. An important finding is that, although the films devoid of Fe were characterized by lower onset overpotentials, their higher Tafel slopes required higher potentials to reach 0.5 mA cm^{-2}. The Ni-based film containing a small amount of Fe produced the optimal catalytic properties (e.g., *a*-$Fe_{20}Ni_{80}O_x$ reached 0.5 mA cm^{-2} at an overpotential at 0.21 V). Overall, the presence of 20−40% Fe in both the binary and the ternary films produced catalysts with the best combination of onset overpotentials and Tafel slopes, enabling the films to achieve 0.5 mA cm^{-2} between 0.21 and 0.25 V. It was found that relative Fe concentrations of >40% in the film had a deleterious effect on catalyst performance due to a loss in onset overpotential.

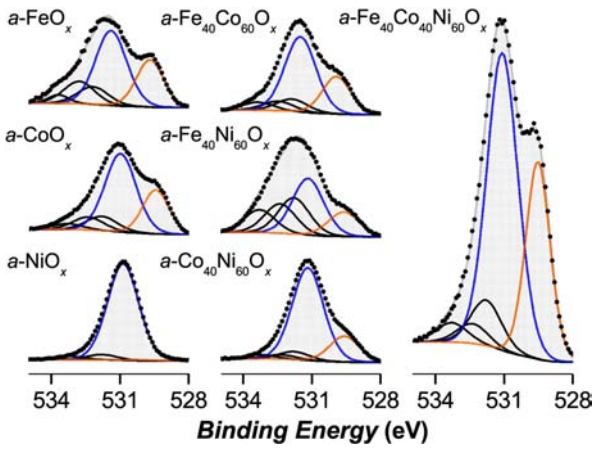

Figure 7. The O1s region of background-corrected photoelectron spectra recorded on the films indicated. Minor peaks from 532 to 534 eV correspond to adventitious carbon−oxygen species (e.g., ethers, esters, ketones, etc.).

SUMMARY

A series of amorphous water oxidation catalysts formulated as *a*-$Fe_{100-y-z}Co_yNi_zO_x$ were prepared by PMOD with precise stoichiometric control. Characterization of the metal oxide films revealed that the predominant metal−oxygen species present in each of the films was sensitive to metal concentrations. A survey of the kinetic parameters revealed the following trends: (i) the presence of small amounts of iron produce a small improvement in overpotential, while iron concentrations of >40% induce a significant increase in overpotential; (ii) despite both *a*-CoO_x and *a*-NiO_x being very good OER catalysts, binary phases of Co and Ni did not produce optimal catalytic behavior; and (iii) moderate amounts (20−40%) of iron in mixed-metal oxide films significantly improves the Tafel slopes. Although *a*-FeO_x is an inferior OER catalyst, the presence of Fe enhances the catalytic properties of the mixed-metal oxide films, a feature that is manifest in stabilizing higher oxidation levels for the collection of metals in the films. This study provides a solid foundation for the systematic study of amorphous mixed-metal OER catalysts.

ASSOCIATED CONTENT

Supporting Information

Description of XPS data fitting procedure, FTIR spectra, XPS survey scans, XPS depth profiles, SEM micrographs, graphical and tabulated fits for high-resolution XPS spectra, comprehensive electrochemical kinetic data, film durability testing using chronopotentiometry, and volcano plot indicating correlation between M−OH content and Tafel slopes. This material is available free of charge via the Internet at http://pubs.acs.org.

AUTHOR INFORMATION

Corresponding Author

trudels@ucalgary.ca; cberling@ucalgary.ca

Notes

The authors declare no competing financial interest.

ACKNOWLEDGMENTS

We thank NSERC, Mitacs, and FireWater Fuel Corp. for financial support. C.P.B. also acknowledges Canadian Research Chairs and the Alfred P. Sloan Foundation for support. This research used facilities funded by the University of Calgary and the Canadian Foundation for Innovation (Leader Opportunity Fund). We thank Robert Marr for running XRD experiments.

REFERENCES

(1) Walter, M. G.; Warren, E. L.; McKone, J. R.; Boettcher, S. W.; Mi, Q.; Santori, E. A.; Lewis, N. S. *Chem. Rev.* **2010**, *110*, 6446−6473.
(2) Cook, T. R.; Dogutan, D. K.; Reece, S. Y.; Surendranath, Y.; Teets, T. S.; Nocera, D. G. *Chem. Rev.* **2010**, *110*, 6474−6502.
(3) Hoare, J. P. *The Electrochemistry of Oxygen*, 1st ed.; John Wiley & Sons, Inc.: New York, 1968.
(4) Lian, K.; Thorpe, S. J.; Kirk, D. W. *Electrochim. Acta* **1992**, *37*, 169−175.
(5) Crousier, J.; Crousier, J. P.; Belucci, F. *Electrochim. Acta* **1993**, *38*, 821−825.
(6) Bockris, J. O.; Otagawa, T. *J. Phys. Chem.* **1983**, *87*, 2960−2971.
(7) Suntivich, J.; May, K. J.; Gasteiger, H. A.; Goodenough, J. B.; Shao-Horn, Y. *Science* **2011**, *334*, 1383−1385.
(8) Merrill, M. D.; Dougherty, R. C. *J. Phys. Chem. C* **2008**, *112*, 3655−3666.
(9) Cattarin, S.; Frateur, I.; Guerriero, P.; Musiani, M. *Electrochim. Acta* **2000**, *45*, 2279−2288.
(10) Kanan, M. W.; Nocera, D. G. *Science* **2008**, *321*, 1072−1075.
(11) Dincă, M.; Surendranath, Y.; Nocera, D. G. *Proc. Natl. Acad. Sci. U.S.A.* **2010**, *107*, 10337−10341.
(12) Blakemore, J. D.; Schley, N. D.; Olack, G. W.; Incarvito, C. D.; Brudvig, G. W.; Crabtree, R. H. *Chem. Sci.* **2011**, *2*, 94−98.
(13) Blakemore, J. D.; Schley, N. D.; Kushner-Lenhoff, M. N.; Winter, A. M.; D'Souza, F.; Crabtree, R. H.; Brudvig, G. W. *Inorg. Chem.* **2012**, *51*, 7749−7763.
(14) Tsuji, E.; Imanishi, A.; Fukui, K.-I.; Nakato, Y. *Electrochim. Acta* **2011**, *56*, 2009−2016.

(15) Marshall, A. T.; Haverkamp, R. G. *Electrochim. Acta* **2010**, *55*, 1978−1984.
(16) Zaharieva, I.; Chernev, P.; Risch, M.; Klingan, K.; Kohlhoff, M.; Fischer, A.; Dau, H. *Energy Environ. Sci.* **2012**, *5*, 7081−7089.
(17) Zaharieva, I.; Najafpour, M. M.; Wiechen, M.; Haumann, M.; Kurz, P.; Dau, H. *Energy Environ. Sci.* **2011**, *4*, 2400−2408.
(18) Yan, H.; Santoso, R. N.; Jiang, Y.; Liang, M. H.; Chen, Z. *Thin Solid Films* **2012**, *520*, 2356−2361.
(19) Avey, A. A.; Hill, R. H. *J. Am. Chem. Soc.* **1996**, *118*, 237−238.
(20) Andronic, L. S.; Hill, R. H. *J. Photochem. Photobiol., A: Chem.* **2002**, *152*, 259−265.
(21) Trudel, S.; Daryl Crozier, E.; Gordon, R. A.; Budnik, P. S.; Hill, R. H. *J. Solid State Chem.* **2011**, *184*, 1025−1035.
(22) Smith, R. D. L.; Prévot, M. S.; Fagan, R. D.; Zhang, Z. Z.; Sedach, P. A.; Siu, M. K. J.; Trudel, S.; Berlinguette, C. P. *Science* **2013**, *340*, 60−63.
(23) Trasatti, S. *Electrochim. Acta* **1984**, *29*, 1503−1512.
(24) Zhu, H. J.; Hill, R. H. *J. Non-Cryst. Solids* **2002**, *311*, 174−184.
(25) Trudel, S.; Li, G.; Zhang, X.; Hill, R. H. *J. Photochem. Photobiol., A: Chem.* **2006**, *19*, 467−475.
(26) Park, H.-H.; Zhang, X.; Lee, S.-W.; Kim, K.-D.; Choi, D.-G.; Choi, J.-H.; Lee, J.; Lee, E.-S.; Park, H.-H.; Hill, R. H.; Jeong, J.-H. *J. Mater. Chem.* **2010**, *21*, 657−662.
(27) Buono-Core, G. E.; Tejos, M.; Lara, J.; Aros, F.; Hill, R. H. *Mater. Res. Bull.* **1999**, *34*, 2333−2340.
(28) White, M. A.; Lovejoy, T. C.; Ochsenbein, S. T.; Olmstead, M. A.; Gamelin, D. R. *J. Appl. Phys.* **2010**, *107*, 103917.
(29) Oswald, S.; Bruckner, W. *Surf. Interface Anal.* **2004**, *36*, 17−22.
(30) McIntyre, N. S.; Zetaruk, D. G. *Anal. Chem.* **1977**, *49*, 1521−1529.
(31) Trotochaud, L.; Ranney, J. K.; Williams, K. N.; Boettcher, S. W. *J. Am. Chem. Soc.* **2012**, *134*, 17253−17261.
(32) Biesinger, M. C.; Payne, B. P.; Grosvenor, A. P.; Lau, L. W. M.; Gerson, A. R.; Smart, R. S. C. *Appl. Surf. Sci.* **2011**, *257*, 2717−2730.
(33) Grosvenor, A. P.; Kobe, B. A.; Biesinger, M. C.; McIntyre, N. S. *Surf. Interface Anal.* **2004**, *36*, 1564−1574.
(34) Biesinger, M. C.; Payne, B. P.; Lau, L. W. M.; Gerson, A.; Smart, R. S. C. *Surf. Interface Anal.* **2009**, *41*, 324−332.
(35) McAlpin, J.; Surendranath, Y.; Dincă, M.; Stich, T.; Stoian, S.; Casey, W.; Nocera, D. G.; Britt, R. D. *J. Am. Chem. Soc.* **2010**, *132*, 6882−6883.
(36) Surendranath, Y.; Kanan, M. W.; Nocera, D. G. *J. Am. Chem. Soc.* **2010**, *132*, 16501−16509.
(37) Gerken, J. B.; Chen, J. Y. C.; Massé, R. C.; Powell, A. B.; Stahl, S. S. *Angew. Chem., Int. Ed.* **2012**, *51*, 6676−6680.